

Herschel*¹ Far-Infrared Spectroscopy of the Galactic Center. Hot Molecular Gas: Shocks versus Radiation near Sgr A

Javier R. Goicoechea², M. Etxaluze², J. Cernicharo², M. Gerin³, D. A. Neufeld⁴,
A. Contursi⁵, T. A. Bell², M. De Luca³, P. Encrenaz³, N. Indriolo⁴,
D. C. Lis⁶, E. T. Polehampton^{7,8}, P. Sonnentrucker⁹

`jr.goicoechea@cab.inta-csic.es`

Received _____; accepted _____

To appear in ApJ Letters

¹*Herschel* is an ESA space observatory with science instruments provided by European-led Principal Investigator consortia and with important participation from NASA.

²Departamento de Astrofísica. Centro de Astrobiología. CSIC-INTA. Carretera de Ajalvir, Km 4. Torrejón de Ardoz, 28850, Madrid, Spain.

³LERMA, UMR 8112 du CNRS, Observatoire de Paris, École Normale Supérieure, France

⁴The Johns Hopkins University, Baltimore, MD 21218, USA

⁵Max-Planck-Institut für extraterrestrische Physik (MPE), Postfach 1312, D-85741 Garching, Germany

⁶California Institute of Technology, Pasadena, CA 91125, USA

⁷RAL Space, Rutherford Appleton Laboratory, Chilton, Didcot, Oxfordshire, OX11 0QX, UK

⁸Institute for Space Imaging Science, University of Lethbridge, 4401 University Drive, Lethbridge, Alberta T1J 1B1, Canada

⁹Space Telescope Science Institute, Baltimore, MD 21218, USA

ABSTRACT

We present a $\sim 52\text{--}671\,\mu\text{m}$ spectral scan toward Sgr A* taken with the PACS and SPIRE spectrometers onboard *Herschel*. The achieved angular resolution allows us to separate, for the first time at far-IR wavelengths, the emission toward the central cavity (gas in the inner central parsec of the galaxy) from that of the surrounding circum-nuclear disk. The spectrum toward Sgr A* is dominated by strong [O III], [O I], [C II], [N III], [N II], and [C I] fine structure lines (in decreasing order of luminosity) arising in gas irradiated by UV-photons from the central stellar cluster. In addition, rotationally excited lines of ^{12}CO (from $J=4\text{--}3$ to $24\text{--}23$), ^{13}CO , H_2O , OH , H_3O^+ , HCO^+ and HCN , as well as ground-state absorption lines of OH^+ , H_2O^+ , H_3O^+ , CH^+ , H_2O , OH , HF , CH and NH are detected. The excitation of the ^{12}CO ladder is consistent with a *hot* isothermal component at $T_{\text{k}} \simeq 10^{3.1}$ K and $n(\text{H}_2) \lesssim 10^4\text{ cm}^{-3}$. It is also consistent with a distribution of temperature components at higher density with most CO at $T_{\text{k}} \lesssim 300$ K. The detected molecular features suggest that, at present, neither very enhanced X-ray, nor cosmic-ray fluxes play a dominant role in the heating of the *hot* molecular gas. The *hot* CO component (either the bulk of the CO column or just a small fraction depending on the above scenario) results from a combination of UV- and shock-driven heating. If irradiated dense clumps/clouds do not exist, shocks likely dominate the heating of the *hot* molecular gas. This is consistent with the high-velocity gas detected toward Sgr A*.

Subject headings: black hole physics — Galaxy: center — infrared: ISM — ISM: molecules, shocks waves

1. Introduction

The Galactic center (GC), in particular the interstellar material in the immediate vicinity (< 5 pc) of the central black hole, represents a unique environment for our understanding of galactic nuclei and galaxy evolution. At a distance $d = 8.0 \pm 0.5$ kpc (Reid 1993), the nucleus of our galaxy is a few hundred times closer than the nearest active galactic nuclei (AGNs), thus allowing high spatial resolution studies. The distribution of gas and dust toward the GC (Genzel et al. 2010) consists of a central cavity of radius ~ 1.5 pc containing warm dust and gas heated and ionized by the central cluster of massive stars orbiting close to the black hole (Sgr A* radio source position). Some of the ionized gas streamers (the “mini-spiral”) bring material close to the very center (Yusef-Zadeh & Morris 1987, see Figure 1).

Between ~ 1.5 pc and ~ 5 pc, a disk of denser molecular gas exists (the circum-nuclear disk or CND; Guesten et al. 1987). However, its density is not well constrained ($\sim 10^4$ - 10^8 cm $^{-3}$) and it is not yet clear whether all the material in the CND is stable against the strong tidal forces in the region or has a more transient nature (Bradford et al. 2005; Montero-Castaño et al. 2009; Requena-Torres et al. 2012). The molecular gas toward the central cavity has been less studied, first because high angular resolution is required to separate the different components and also because column densities are inevitably lower and emission lines are intrinsically weak. Nevertheless, the detection of CO ro-vibrational lines in absorption (Moneti et al. 2001) and of broad NH $_3$ (6,6) emission lines close to Sgr A* (Herrnstein & Ho 2002) suggests that *hot* molecular gas must exist interior to the CND.

Owing to the lower dust extinction at far-IR wavelengths and because of the strong emission from the interstellar component related to AGN and star formation activity, the relevance of far-IR spectroscopy to characterize extragalactic nuclei has notably increased

(*e.g.*, van der Werf et al. 2010). The far-IR spectrum of the Milky Way’s nucleus is obviously a key template.

The angular resolution achieved by the *Herschel Space Observatory* ($\sim 10'' - 40''$; Pilbratt et al. 2010) allows us to separate the emission of the central cavity from the CND. In this *Letter* we present initial results from a *Herschel* far-IR spectroscopic study of the GC. We present the complete PACS (Poglitsch et al. 2010) and SPIRE (Griffin et al. 2010) spectra toward Sgr A* that are part of the PRISMAS and SPECHIS Guaranteed-Time Programs. We discuss the properties and possible origin of the atomic and of the *hot* molecular gas.

2. Observations and Data Reduction

PACS spectra between ~ 52 and $\sim 190 \mu\text{m}$ were obtained during 2011 March and 2012 March. The PACS spectrometer provides 25 spectra over a $47'' \times 47''$ field-of-view (FoV) resolved in 5×5 “spaxels”, each with a size of $\sim 9.4''$. The resolving power varies between $R = \lambda / \Delta\lambda \simeq 1000$ at $\sim 100 \mu\text{m}$ and $R \simeq 5000$ at $\sim 70 \mu\text{m}$. The central spaxel was centered on Sgr A* (α_{2000} : $17^h 45^m 40.04^s$, δ_{2000} : $-29^\circ 00' 28.19''$). The observations were carried out in the “unchopped” mode (IDs 1342217802 and 342242442). Background subtraction was achieved by removing the telescope background spectrum measured on a distant off-position. The observing time was ~ 2.4 hr. The measured width of the point spread function is relatively constant for $\lambda \lesssim 100 \mu\text{m}$ (\sim spaxel size) but increases at longer wavelengths. In particular only $\simeq 40\%$ of a point source emission would fall in the central spaxel at $\simeq 190 \mu\text{m}$. Therefore, owing to the extended nature of the emission, the flux measured by a single spaxel cannot be used individually. Instead, we added the 3×3 central spaxels ($\sim 30'' \times 30''$).

SPIRE-FTS observations between ~ 194 and $\sim 671 \mu\text{m}$ were obtained during 2011

February (ID1342214845). The SPIRE-FTS uses two bolometer arrays covering the 194-313 μm and 303-671 μm bands at 0.04 cm^{-1} resolution ($R \simeq 500\text{-}1000$). The two arrays contain 19 and 37 detectors separated by ~ 2 beams ($51''$ and $33''$ respectively). The unvignetted FoV is $\sim 2'$. The observing time was 798 s. The *Herschel* data were processed with HIPE 9.2. Table 1 summarizes the atomic and CO line intensities obtained in a $\sim 30'' \times 30''$ aperture.

3. Results: Spectroscopy

Figure 1a shows the CO $J=13\text{-}12$ line intensity map of the central ~ 4 pc of the Galaxy displaying extended excited CO emission that peaks toward the northern and southern lobes of the CND (hereafter *N*-CND and *S*-CND). Figures 1b, c and d show the CO $J=19\text{-}18$, [N III] 57 and [O I] 63 μm line spectral-maps respectively.

Figure 2 shows the complete $\sim 52\text{-}671\text{ }\mu\text{m}$ spectrum toward Sgr A* (black curves) and toward a bright position at the inner edge of the *S*-CND, ~ 1 pc from Sgr A* (only for PACS; gray curves). The far-IR spectrum toward Sgr A* is dominated by strong emission from atomic fine structure lines ([O III], [O I], [C II], [N III], [N II], and [C I]), high- J CO rotational lines (up to $J=24\text{-}23$ toward the central cavity and up to $J=30\text{-}29$ in the CND), mid- J HCO⁺ and HCN emission lines and ground-state absorption lines from light hydrides (OH⁺, H₂O⁺, H₃O⁺, CH⁺, HF, CH, NH, OH and H₂O). Among the molecular ions, only H₃O⁺ shows absorption lines from excited levels (metastable levels up to $J_K=6_6$ toward the central cavity). The detection of rotationally excited lines from H₂O, OH and H₃O⁺ in absorption, suggests that a non negligible fraction of excited molecular gas resides at relatively low densities.

Owing to the $A_V \simeq 30$ mag of extinction toward the GC (Genzel et al. 2010), in the

following discussion we correct all line intensities ($I_0 = C_\lambda I_{\text{obs}}$) using an extrapolation of the mid-IR extinction-law derived by Lutz (1999) for Sgr A*. These corrections are $<15\%$ in the far-IR (Table 1). The corrected line luminosities in the inner $\sim 30'' \times 30''$ (~ 0.6 pc in radius) are¹ $L_{[\text{OIII}]} \simeq 885 L_\odot$, $L_{[\text{OI}]} \simeq 855 L_\odot$, $L_{[\text{CII}]} \simeq 230 L_\odot$, $L_{[\text{NIII}]} \simeq 130 L_\odot$, $L_{[\text{NII}]} \simeq 120 L_\odot$, $L_{12\text{CO}} \simeq 125 L_\odot$, $L_{13\text{CO}} \simeq 4 L_\odot$ and $L_{[\text{CI}]} \simeq 6 L_\odot$ (adopting $d=8$ kpc).

3.1. Ionized Gas and Neutral Atomic Gas

The velocity resolution of PACS spectra at short wavelengths, $\lesssim 100 \text{ km s}^{-1}$, allows one to resolve shifts in the line profile peak velocity if they are large. Figures 1c and d show the [O I] 63 and [N III] 57 μm line maps. The Doppler shifts of both lines reveal motions of the neutral and of the ionized gas, with blueshifted velocities observed toward the S-CND and redshifted toward the N-CND. The [N III] 57 μm lines show a similar pattern to the [Ne II] 13 μm lines observed at higher spatial and spectral resolution (Irons et al. 2012). They are consistent with ionized gas streamers orbiting or falling in a potential dominated by the central black hole (Serabyn & Lacy 1985; Paumard et al. 2004). Note that both the [O I] 63 and [N III] 57 μm lines show high-velocity wing emission ($\gtrsim \pm 300 \text{ km s}^{-1}$) toward Sgr A* and narrower profiles at greater distances from the center. This high-velocity gas is likely associated with clouds/clumps moving fast and close to Sgr A*.

The spatial distribution of the [N III] lines follows the dense filaments ($n_e > 10^{3.5} \text{ cm}^{-3}$) of ionized gas orbiting Sgr A* (the mini-spiral shown in Figure 1, Yusef-Zadeh & Morris 1987). This lower limit to the electron density (n_e) is estimated by comparing the [O III] 88-to-[O III] 52 line intensity ratio of 0.21 ± 0.12 (hereafter [O III] 88/52) with the

¹We obtain $L_{\text{FIR}}(50\text{-}1000 \mu\text{m}) \simeq 10^{5.1} L_\odot$ using *Herschel* photometric data from Etxaluze et al. (2011).

semi-empirical prescription of Rubin et al. (1994).

The [N III] 57 and [N II] 122 μm line intensities can also be used to estimate the effective temperature of the ionizing radiation (T_{eff}) for a given n_e (Rubin et al. 1994). The [N III] 57/[N II] 122 = 1.31 ± 0.51 intensity ratio toward Sgr A* results in $T_{\text{eff}} \simeq 35,000 \pm 1000$ K (see Shields & Ferland 1994, for photoionization detailed models).

The strong UV radiation field from stars in the central parsec is thought to dominate the heating of the dust grains and of the neutral atomic gas (Genzel et al. 1985; Jackson et al. 1993). The low $(L_{[\text{OI}]} + L_{[\text{CII}]})/L_{\text{FIR}} \simeq 8 \times 10^{-3}$ luminosity ratio toward the central cavity agrees with the low efficiency heating mechanisms expected in photodissociation regions (PDRs). In addition, [O I] 63/[C II] 158 = 3.32 ± 1.31 and [O I] 145/63 = 0.12 ± 0.05 line intensity ratios are observed toward Sgr A*. These are similar to the ratios observed in strongly irradiated PDRs like the Orion Bar (Bernard-Salas et al. 2012) but are significantly lower than the expected ratios in shocked gas and in X-ray dominated regions (XDRs; Maloney et al. 1996). Therefore, the neutral atomic gas ($n_{\text{H}} \sim 10^{4-5} \text{ cm}^{-3}$) is predominantly heated by UV photons ($G_0 > 10^4$ times the mean interstellar radiation field). Atomic gas temperatures $\lesssim 500$ K are expected in this PDR range (Wolfire et al. 1990). Nevertheless, narrow (unresolved) absorption components from foreground gas in the GC (*e.g.*, Sonnentrucker et al. 2013) can affect the total [O I] 63 and [C II] 158 μm fluxes measured by PACS at medium spectral resolution (both are ground-state transitions). Hence, the actual ratios may be different, and our unresolved [O I] and [C II] intensities may have less diagnostic power.

3.2. Hot Molecular Gas

Figure 3a shows all detected ^{12}CO lines toward the central cavity on a *rotational diagram* that assumes extended emission. The average $^{12}\text{CO}/^{13}\text{CO}$ line intensity ratio is 22 ± 9 (lines $J=5-4$ to $10-9$), thus consistent with the $^{12}\text{C}/^{13}\text{C} \simeq 20-25$ isotopic ratio inferred in the Sgr A complex (Penzias 1980). Hence, the observed line intensity ratios are compatible with optically thin ^{12}CO line emission (see the next section).

By fitting the ^{12}CO lines detected by SPIRE and PACS independently, we obtain $T_{\text{rot}}(\text{SPIRE}) \simeq 87 \text{ K}$ and $T_{\text{rot}}(\text{PACS}) \simeq 232 \text{ K}$ respectively. T_{rot} is a good measure of the gas temperature only in the high density limit (close to *local thermodynamic equilibrium*, LTE). In this case, the two slopes could be associated with two different temperature components, the hotter one representing $\lesssim 4\%$ of the total ^{12}CO column density. Alternatively, T_{rot} can reflect much higher gas temperatures if the density is significantly lower than the critical density for collisional excitation ($n_{\text{cr}}(\text{H}_2) > 10^7 \text{ cm}^{-3}$ for the observed high- J lines).

In fact, a closer inspection of the rotational diagram shows that T_{rot} increases with J , from $T_{\text{rot}}(14-18) \simeq 160 \text{ K}$ to $T_{\text{rot}}(19-24) \simeq 250 \text{ K}$. Therefore, the rotational diagram shows a moderate *positive curvature* and thus even a single temperature component in LTE cannot explain the CO emission detected by PACS. Neufeld (2012) pointed out that a moderate positive curvature can be explained either by (1) a *subthermally excited* single temperature component ($T_{\text{k}} \gg T_{\text{rot}}$) or (2) multiple-temperature components (that could be in LTE).

In order to constrain the range of physical conditions that reproduce the observed CO intensities, we have run a grid of non-local, non-LTE isothermal models (Goicoechea et al. 2006) using $^{12}\text{CO}-\text{H}_2$ collisional rates from Yang et al. (2010). We used a constant beam-averaged CO column density, $N(\text{CO})$, and a nonthermal velocity dispersion $\sigma = 65 \text{ km s}^{-1}$ (from turbulence and macroscopic gas motions), implying $\Delta v \simeq 150 \text{ km s}^{-1}$ line-widths. These broad widths are consistent with the mid- J CO

line-widths observed with *Herschel*/HIFI (T.A. Bell 2013, private communication). We adopt $N(\text{CO}) = \chi(\text{CO}) \times N(\text{H}_2) = 10^{18} \text{ cm}^{-2}$ (Genzel et al. 1985), *i.e.*, we assume a CO abundance of $\simeq 10^{-4}$ and take, from photometric measurements, $N(\text{H}_2) \simeq 10^{22} \text{ cm}^{-2}$ ($A_V \sim 10$) in the central cavity (Etxaluze et al. 2011).

Figure 3*b* shows the model results in the form of iso- T_{rot} contours. To make this plot, we first created rotational diagrams from each model and determined T_{rot} by fitting a straight line to the synthetic CO line intensities in the $J_{\text{up}} = 16\text{--}24$ range. Figure 3*b* shows that in terms of excitation alone, the same $T_{\text{rot}}(\text{PACS}) \approx 232 \text{ K}$ can be obtained for different combinations of density and temperature. In a second step, we searched for the range of $n(\text{H}_2)$ and T_{k} values that better reproduce the observed ^{12}CO lines by fitting their absolute intensities. For the adopted $N(\text{CO})$, the best-fit parameters are obtained around $T_{\text{k}} \simeq 10^{3.1} \text{ K}$ and $n(\text{H}_2) \simeq 10^{3.7} \text{ cm}^{-3}$. The resulting best-fit rotational diagram is shown as a green curve in Figure 3*a* (note that it is also consistent with the 3σ upper limits for higher- J undetected lines).

In a third step, we compared the observations with the more extensive model grid of Neufeld (2012) and studied the dependence of our results on the assumed $N(\text{CO})$. For isothermal models, the gas temperature is well constrained and $T_{\text{k}} \simeq 10^{3.1} \text{ K}$ reproduces the observed CO rotational ladder (also the lines detected by PACS alone) independently of the assumed $N(\text{CO})$. Even lower densities (for less realistic higher $N(\text{CO})$ columns) can also reproduce the CO ladder.

In addition to the isothermal solution, multiple gas temperature components can also explain a CO rotational diagram with positive curvature. Neufeld (2012) studied the case of a medium with a power-law distribution of temperatures, $dN(\text{CO})/dT_{\text{k}} = aT_{\text{k}}^{-b}$. Including all CO lines observed by *Herschel* in the fit gives $b \simeq 2.0 - 2.5$ and $n(\text{H}_2) \simeq 10^{4-5} \text{ cm}^{-3}$. In other words, although a small fraction of the total ^{12}CO column exists at $T_{\text{k}} > 300 \text{ K}$ ($\lesssim 4\%$),

most of the $N(\text{CO})$ column will be at lower temperatures and higher densities than those implied by the isothermal solution. We therefore conclude that the observed CO lines are consistent with either a single, *hot* ($T_k \simeq 10^{3.1}$ K), low-density ($n(\text{H}_2) \lesssim 10^4 \text{ cm}^{-3}$) component, or with multiple, cooler components at a higher density. In the latter case, the required density will be above the beam-averaged gas densities in the central cavity ($\sim 10^{3-4} \text{ cm}^{-3}$; Etxaluze et al. 2011), implying that the *hot molecular gas* in the vicinity of Sgr A* does not have a homogeneous distribution but fills a small fraction of the volume.

4. Discussion

In this section we discuss the possible heating mechanisms of the *hot* molecular gas toward the central parsec. In order to evaluate the role of UV radiation in the heating and excitation of CO, we used an updated version of the *Meudon* PDR code (Le Boulrot et al. 2012) to compute synthetic CO rotational diagrams for the integrated CO emission from $A_V=0$ to 10. We adopted $G_0=10^{4.9}$ (Wolfire et al. 1990) and different gas densities. Our photochemical model includes selective photodissociation of CO-isotopologues and ^{13}C fractionation. For the considered range of densities, selective photodissociation slightly increases the $^{12}\text{CO}/^{13}\text{CO}$ column density ratio over the $^{12}\text{C}/^{13}\text{C}$ isotopic ratio (by $\lesssim 25\%$) at the $A_V < 2$ surface layers where CO columns are still low. Deeper inside, as the gas temperature decreases, ^{13}C isotope exchange starts to be important and the $^{12}\text{CO}/^{13}\text{CO}$ column density ratio can be lower than the $^{12}\text{C}/^{13}\text{C}$ ratio. All in all, we conclude that the beam-averaged $N(^{12}\text{CO})$ toward Sgr A* cannot be much larger than the adopted $\sim 10^{18} \text{ cm}^{-2}$. For these columns and large velocity dispersions, the observed ^{12}CO lines are optically thin. Figure 3a shows the resulting CO diagrams for different PDR models and filling factors. By comparing with observations, we see that low-density PDRs ($n_{\text{H}} \leq 10^5 \text{ cm}^{-3}$) are not able to reproduce the high- J CO emission and an extra heating/excitation source is

needed. In addition to photoelectric heating, denser PDRs ($n_{\text{H}} \simeq 10^{6-7} \text{ cm}^{-3}$) heat larger columns of molecular gas (to $T_{\text{k}} \sim 10^3 \text{ K}$) by vibrational heating from collisional deexcitation of UV-pumped H_2 molecules. Therefore, in addition to an extended low-density medium, a small filling factor ensemble of irradiated dense clumps/clouds could be responsible of the high- J CO emission (Burton et al. 1990). Our best combined PDR models, however, do not provide an entirely satisfactory fit of the CO rotational ladder. This result is consistent with the lack of good high-density fits to the high- J CO lines (see previous the section) and suggests that UV radiation alone can not heat the *hot* molecular gas.

Interestingly, the SPIRE-FTS spectrum toward Sgr A* resembles that of the M82 starburst galaxy (Kamenetzky et al. 2012). However, the *hot* CO rotational temperatures inferred toward Sgr A* are significantly higher than those seen in strongly irradiated PDRs like the Orion Bar, which shows a rotational diagram (up to $J=21-20$) that can be fitted with a single $T_{\text{rot}}(\text{CO}) \simeq 150 \text{ K}$ component (Habart et al. 2010, C. Joblin et al. in preparation). In addition, even toward the strongly UV-irradiated central cavity, the observed $L(\text{CO})/L_{\text{FIR}} \simeq 10^{-3}$ luminosity ratio is higher than the expected ratio in PDRs and XDRs models (Meijerink et al. 2013), and it is indeed higher than the observed value in the Orion Bar ($L(\text{CO})/L_{\text{FIR}} \simeq 3 \times 10^{-4}$; C. Joblin 2013, private communication).

The current X-ray luminosity near Sgr A* is rather low ($L_{\text{X}}(2-120 \text{ keV}) < 10^{36} \text{ erg s}^{-1}$; Bélanger et al. 2006), far lower than that expected from black hole accretion models. Hence, any incident X-ray flux at a typical distance of $\sim 0.5 \text{ pc}$ from the source ($F_{\text{X}} < 0.03 \text{ erg cm}^{-2} \text{ s}^{-1}$) would be too low to heat a significant fraction of the molecular gas well above $T_{\text{k}} \sim 100 \text{ K}$ (Maloney et al. 1996).

High cosmic-ray (CR) ionization rates ($\zeta_{\text{CR}} \gtrsim 10^{-15} \text{ s}^{-1}$) have been inferred in the GC region from H_3^+ observations, and even higher rates have been proposed for the vicinity of Sgr A* ($\sim 2 \times 10^{-14} \text{ s}^{-1}$; Goto et al. 2008). At least qualitatively, our detection

of H_3O^+ absorption lines from excited metastable levels indeed suggests that ζ_{CR} may be high. Nevertheless, the ionization fraction of the molecular gas in the central parsec seems lower than that in much more extreme X-ray dominated AGNs like Mrk 231 ($L_{\text{X}}(2\text{-}10\text{ keV}) \simeq 6 \times 10^{43} \text{ erg s}^{-1}$), where strong CH^+ , OH^+ and H_2O^+ emission lines have been detected (van der Werf et al. 2010). It also has to be lower than in the ULIRG galaxy Arp 220, where the detection of many excited OH^+ and H_2O^+ absorption lines has been associated with very enhanced X-ray/CR ionization rates ($\zeta_{\text{X,CR}} > 10^{-13} \text{ s}^{-1}$; González-Alfonso et al. 2013). Our observations toward Sgr A* show that OH^+ and H_2O^+ only produce appreciable ground-state absorption lines, and they are known to arise from semi-atomic diffuse clouds, where their columns are proportional to ζ_{CR} (Gerin et al. 2010; Neufeld et al. 2010; Hollenbach et al. 2012). Hence, ζ_{CR} toward Sgr A* is very likely higher than in Galactic disk clouds, but lower than $\zeta_{\text{X,CR}}$ in Mrk 231 or Arp 220. Simple thermodynamic considerations show that even $\zeta_{\text{CR}} = 2 \times 10^{-14} \text{ s}^{-1}$ would only heat the gas to a few tens of K (see also Glassgold et al. 2012). Therefore, neither X-rays nor CRs presently dominate the heating of the *hot* molecular gas near Sgr A*.

Low-density shocks (and related supersonic turbulence dissipation and magnetic viscous heating) are promising candidates in the highly magnetized GC environment (Morris & Serabyn 1996). In particular, non-dissociative, magnetohydrodynamic shocks tend to produce regions that are roughly isothermal, reaching very high temperatures without destroying molecules ($T_{\text{k}} > 1000 \text{ K}$ for shock velocities $v_{\text{s}} > 20 \text{ km s}^{-1}$ in C-type shock models by Kaufman & Neufeld 1996). In fact, shocks with a variety of densities, v_{s} and magnetic field strengths dominate the heating of the hot molecular gas seen in protostellar outflows (with $L(\text{CO})/L_{\text{FIR}} \simeq 2 \times 10^{-3}$ observed in Serpens SMM1; Goicoechea et al. 2012). Hence, the *hot* CO gas inferred toward Sgr A*, the high $L(\text{CO})/L_{\text{FIR}}$ ratio and the almost thermal H_2 rovibrational spectrum (Tanaka et al. 1989) suggest that, in addition to UV-driven excitation, shocks *contribute* to the heating of the *hot* molecular gas in the nucleus of the

Galaxy. Indeed, if a small filling factor ensemble of dense clumps/clouds does not exist, shocks likely *dominate*.

Whether the required shocks are produced within high-velocity molecular gas falling toward the very center region (Gillesen et al. 2012), arise in clump-clump collisions (Martín-Pintado et al. 1997) or in outflows driven by high-velocity stellar winds (Najarro et al. 1997) or by protostars in the central parsec (Nishiyama & Schödel 2013) is still uncertain.

We thank C. Lang and M.A. Requena-Torres for providing us with the VLA 6 cm radiocontinuum image in CLASS format, and C. Joblin and O. Berné for useful discussions on the Orion Bar. We thank the Spanish MINECO for funding support from grants AYA2009-07304, CSD2009-00038 and S2009ESP-1496, and NASA through an award issued by JPL/Caltech. J.R.G. is supported by a *Ramón y Cajal* research contract.

REFERENCES

- Bélanger, G., Glowworm, A., Renaud, M., et al. 2006, *ApJ*, 636, 275
- Bernard-Salas, J., Habart, E., Arab, H., et al. 2012, *A&A*, 538, A37
- Bradford, C. M., Stacey, G. J., Nikola, T., et al. 2005, *ApJ*, 623, 866
- Burton, M. G., Hollenbach, D. J., & Tielens, A. G. G. M. 1990, *ApJ*, 365, 620
- Etxaluze, M., Smith, H. A., Tolls, V., Stark, A. A., & González-Alfonso, E. 2011, *AJ*, 142, 134
- Genzel, R., Crawford, M. K., Townes, C. H., & Watson, D. M. 1985, *ApJ*, 297, 766
- Genzel, R., Eisenhauer, F., & Gillessen, S. 2010, *Reviews of Modern Physics*, 82, 3121
- Gerin, M., de Luca, M., Black, J., et al. 2010, *A&A*, 518, L110
- Gillessen, S., Genzel, R., Fritz, T. K., et al. 2012, *Nature*, 481, 51
- Glassgold, A. E., Galli, D., & Padovani, M. 2012, *ApJ*, 756, 157
- Goicoechea, J. R., Cernicharo, J., Karska, A., et al. 2012, *A&A*, 548, A77
- Goicoechea, J. R., Pety, J., Gerin, M., et al. 2006, *A&A*, 456, 565
- González-Alfonso, E., Fischer, J., Bruderer, S., et al. 2013, *A&A*, 550, 25
- Goto, M., Usuda, T., Nagata, T., et al. 2008, *ApJ*, 688, 306
- Griffin, M. J., Abergel, A., Abreu, A., et al. 2010, *A&A*, 518, L3
- Guesten, R., Genzel, R., Wright, M. C. H., et al. 1987, *ApJ*, 318, 124
- Habart, E., Dartois, E., Abergel, A., et al. 2010, *A&A*, 518, L116

- Herrnstein, R. M., & Ho, P. T. P. 2002, ApJ, 579, L83
- Hollenbach, D., Kaufman, M. J., Neufeld, D., Wolfire, M., & Goicoechea, J. R. 2012, ApJ, 754, 105
- Irons, W. T., Lacy, J. H., & Richter, M. J. 2012, ApJ, 755, 90
- Jackson, J. M., Geis, N., Genzel, R., et al. 1993, ApJ, 402, 173
- Kamenetzky, J., Glenn, J., Rangwala, N., et al. 2012, ApJ, 753, 70
- Kaufman, M. J., & Neufeld, D. A. 1996, ApJ, 456, 611
- Le Bourlot, J., Le Petit, F., Pinto, C., Roueff, E., & Roy, F. 2012, A&A, 541, A76
- Lutz, D. 1999, *The Universe as Seen by ISO*, 427, 623
- Maloney, P. R., Hollenbach, D. J., & Tielens, A. G. G. M. 1996, ApJ, 466, 561
- Martín-Pintado, J., de Vicente, P., Fuente, A., & Planesas, P. 1997, ApJ, 482, L45
- Meijerink, R., Kristensen, L. E., Weiß, A., et al. 2013, ApJ, 762, L16
- Moneti, A., Cernicharo, J., & Pardo, J. R. 2001, ApJ, 549, L203
- Montero-Castaño, M., Herrnstein, R. M., & Ho, P. T. P. 2009, ApJ, 695, 1477
- Morris, M., & Serabyn, E. 1996, ARA&A, 34, 645
- Najarro, F., Krabbe, A., Genzel, R., et al. 1997, A&A, 325, 700
- Neufeld, D. A. 2012, ApJ, 749, 125
- Neufeld, D. A., Goicoechea, J. R., Sonnentrucker, P., et al. 2010, A&A, 521, L10
- Nishiyama, S., & Schödel, R. 2013, A&A, 549, A57

- Paumard, T., Maillard, J.-P., & Morris, M. 2004, *A&A*, 426, 81
- Penzias, A. A. 1980, *Science*, 208, 663
- Pilbratt, G. L., Riedinger, J. R., Passvogel, T., et al. 2010, *A&A*, 518, L1
- Poglitsch, A., Waelkens, C., Geis, N., et al. 2010, *A&A*, 518, L2
- Reid, M. J. 1993, *ARA&A*, 31, 345
- Requena-Torres, M. A., Güsten, R., Weiß, A., et al. 2012, *A&A*, 542, L21
- Rubin, R. H., Simpson, J. P., Lord, S. D., et al. 1994, *ApJ*, 420, 772
- Serabyn, E., & Lacy, J. H. 1985, *ApJ*, 293, 445
- Shields, J. C., & Ferland, G. J. 1994, *ApJ*, 430, 236
- Sonnentrucker, P., Neufeld, D. A., Gerin, M., De Luca, M., Indriolo, N., Lis, D. C. , & Goicoechea, J.R. 2013, *ApJ*, 763, L19
- Tanaka, M., Hasegawa, T., Hayashi, S. S., Brand, P. W. J. L., & Gatley, I. 1989, *ApJ*, 336, 207
- van der Werf, P. P., Isaak, K. G., Meijerink, R., et al. 2010, *A&A*, 518, L42
- Wolfire, M. G., Tielens, A. G. G. M., & Hollenbach, D. 1990, *ApJ*, 358, 116
- Yang, B., Stancil, P. C., Balakrishnan, N., & Forrey, R. C. 2010, *ApJ*, 718, 1062
- Yusef-Zadeh, F., & Morris, M. 1987, *ApJ*, 320, 545

Table 1. Atomic and CO Line Intensities Toward Sgr A*

Species	Transition	$\lambda(\mu\text{m})$	E_u/k (K)	I_{obs}^a	C_λ^b
[O III]	$^3P_2 - ^3P_1$	51.815	441	1.52E-05 ^c	1.152
[N III]	$^2P_{3/2} - ^2P_{1/2}$	57.317	251	2.69E-06	1.132
[O I]	$^3P_1 - ^3P_2$	63.184	228	1.62E-05	1.116
[O III]	$^3P_1 - ^3P_0$	88.356	163	3.30E-06	1.076
[N II]	$^3P_2 - ^3P_1$	121.898	188	2.21E-06	1.051
[O I]	$^3P_0 - ^3P_1$	145.525	327	2.11E-06	1.041
[C II]	$^2P_{3/2} - ^2P_{1/2}$	157.741	91	5.26E-06	1.037
[N II]	$^3P_1 - ^3P_0$	205.178	70	4.51E-07	1.026
[C I]	$^3P_2 - ^3P_1$	370.414	63	1.22E-07	1.013
[C I]	$^3P_1 - ^3P_0$	609.133	24	1.95E-08	1.007
¹² CO	$J=24-23$	108.763	1656.6	1.40E-08	1.058
¹² CO	$J=23-22$	113.458	1524.3	3.49E-08 ^d	1.055
¹² CO	$J=22-21$	118.581	1397.4	2.37E-08	1.052
¹² CO	$J=21-20$	124.193	1276.1	3.95E-08	1.049
¹² CO	$J=20-19$	130.369	1160.3	3.58E-08	1.047
¹² CO	$J=19-18$	137.196	1049.9	5.26E-08	1.044
¹² CO	$J=18-17$	144.784	945.0	4.67E-08	1.041
¹² CO	$J=17-16$	153.267	845.6	5.23E-08	1.038
¹² CO	$J=16-15$	162.812	751.8	7.54E-08	1.035
¹² CO	$J=15-14$	173.631	663.4	9.66E-08	1.032
¹² CO	$J=14-13$	185.999	580.5	1.30E-07	1.030
¹² CO	$J=13-12$	200.272	503.2	1.59E-07	1.027
¹² CO	$J=12-11$	216.927	431.3	1.94E-07	1.025
¹² CO	$J=11-10$	236.613	365.0	2.38E-07	1.022
¹² CO	$J=10-9$	260.240	304.2	2.75E-07	1.020
¹² CO	$J=9-8$	289.120	248.9	2.84E-07	1.017
¹² CO	$J=8-7$	325.225	199.1	3.89E-07	1.015
¹² CO	$J=7-6$	371.650	154.9	3.08E-07	1.013
¹² CO	$J=6-5$	433.556	116.2	2.02E-07	1.011
¹² CO	$J=5-4$	520.231	83.0	1.34E-07	1.009
¹² CO	$J=4-3$	650.252	55.3	7.81E-08	1.007
¹³ CO	$J=12-11$	226.898	412.4	6.53E-09	1.023
¹³ CO	$J=11-10$	247.490	348.9	6.68E-09	1.021
¹³ CO	$J=10-9$	272.205	290.8	8.52E-09	1.019
¹³ CO	$J=9-8$	302.415	237.9	1.94E-08	1.016
¹³ CO	$J=8-7$	340.181	190.4	2.00E-08	1.014
¹³ CO	$J=7-6$	388.743	148.1	1.63E-08	1.012
¹³ CO	$J=6-5$	453.498	111.1	6.25E-09	1.010
¹³ CO	$J=5-4$	544.161	79.3	1.08E-08	1.008

^aObserved lines intensities above 3σ in $\text{W m}^{-2} \text{sr}^{-1}$. Absolute calibration accuracy up to $\sim 30\%$.

^bExtinction correction factors. ^cFrom Shields & Ferland (1994).

^dBlended with the $o\text{-H}_2\text{O } 4_{14}\text{-}3_{03}$ line.

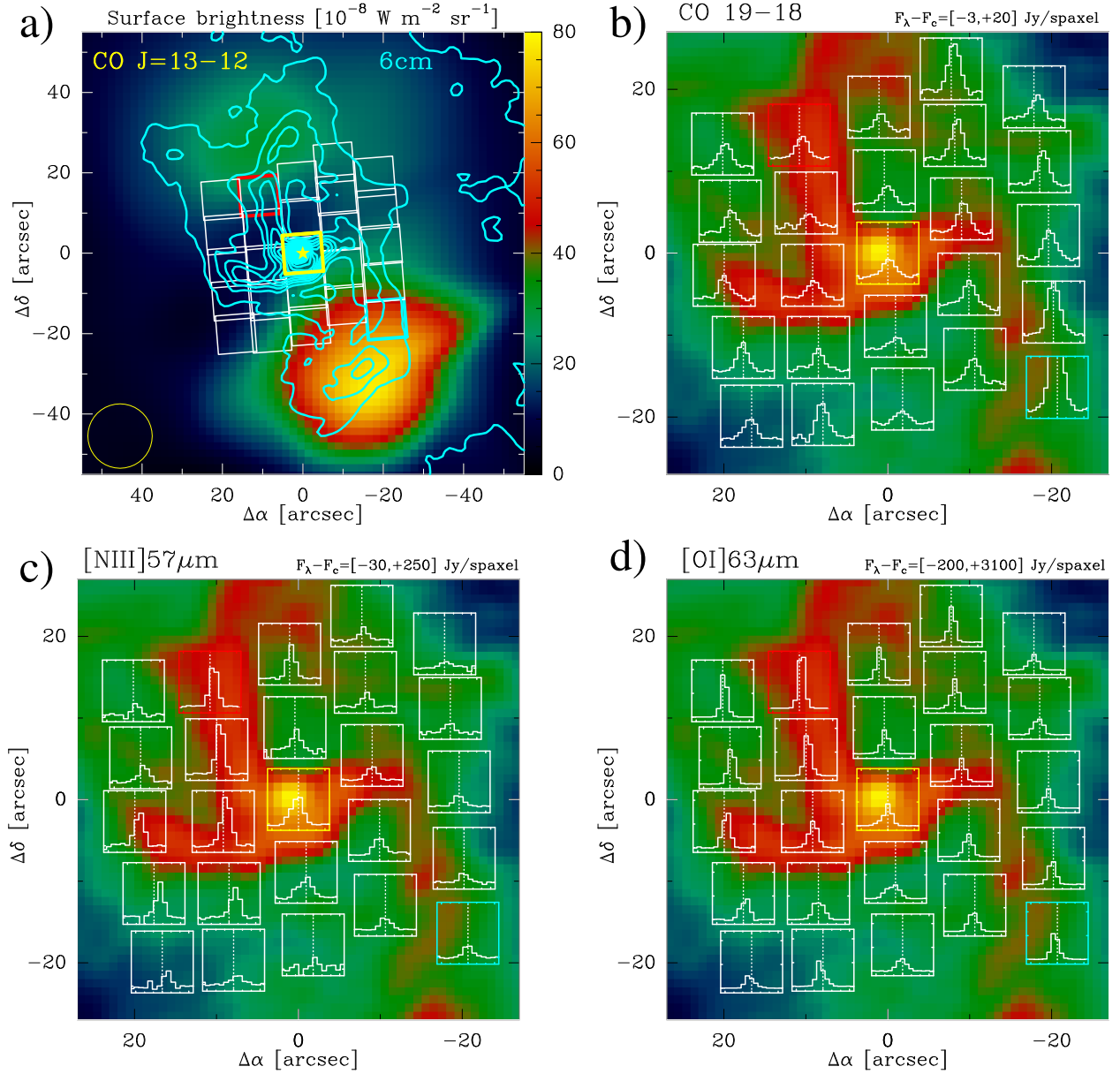


Fig. 1.— (a) SPIRE-FTS ^{12}CO $J=13-12$ sparse-sampling map of the GC and VLA 6cm radio continuum showing ionized gas in the mini-spiral (cyan contours, Yusef-Zadeh & Morris 1987). Sgr A* is marked with a star. The PACS footprint is overplotted. Panels (b), (c) and (d): PACS continuum-subtracted maps for the CO $J=19-18$ ($137.196 \mu\text{m}$), [N III] $57.317 \mu\text{m}$ and [O I] $63.183 \mu\text{m}$ lines. The center of each spaxel corresponds to its offset position with respect to Sgr A*. The X-axis represents the -700 to $+700 \text{ km s}^{-1}$ velocity scale. The line flux scale (Y-axis) is shown in each map. The 6cm radio continuum image is shown in the background.

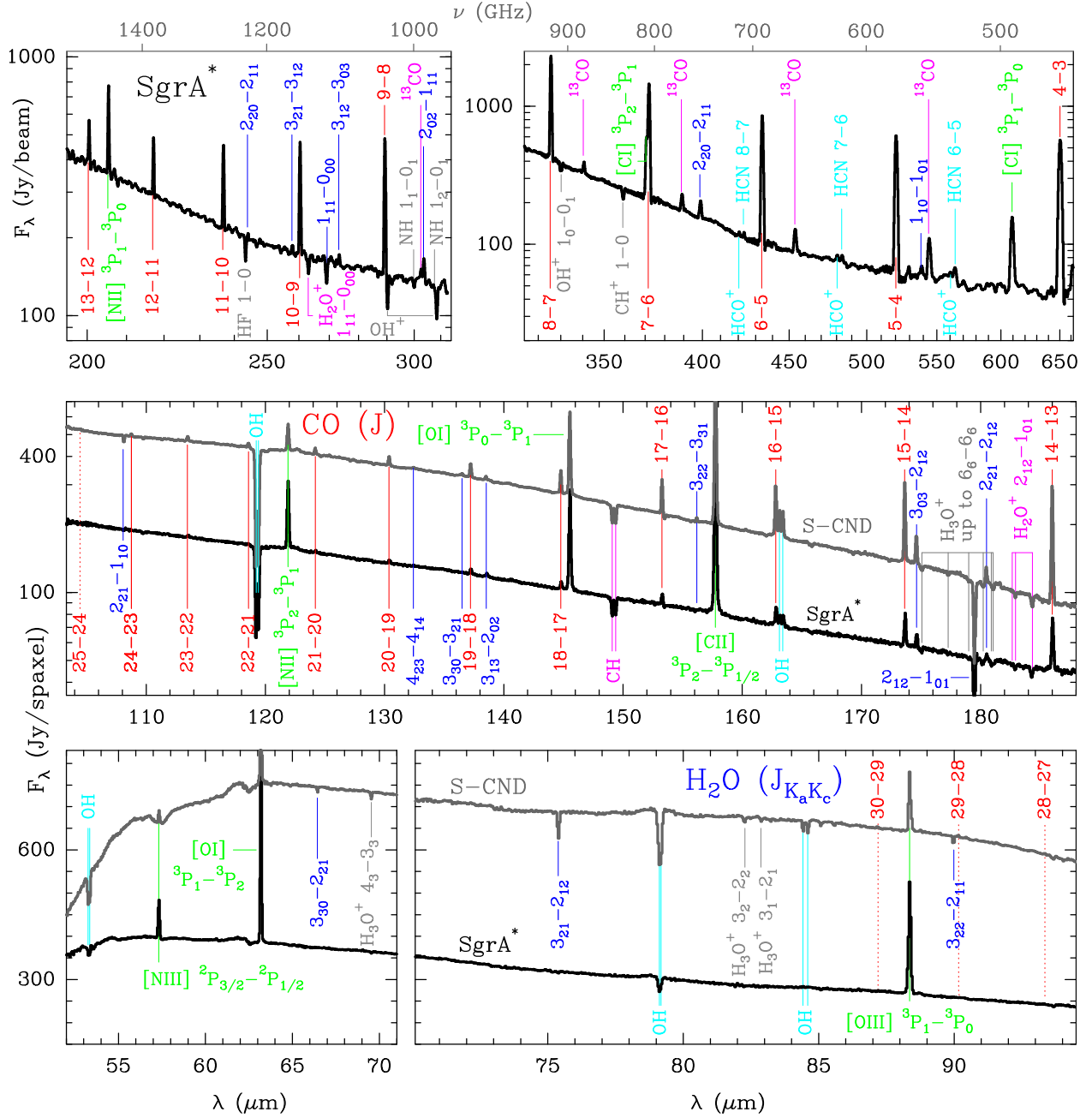


Fig. 2.— *Top* panel: SPIRE-FTS spectrum toward Sgr A*. *Middle* and *bottom* panels: PACS spectra toward Sgr A* (black curves; yellow spaxel in Fig. 1a) and also toward the S-CND (gray curves; blue spaxel in Fig. 1a). Flux density units are Jy spaxel⁻¹ for PACS and Jy beam⁻¹ for SPIRE.

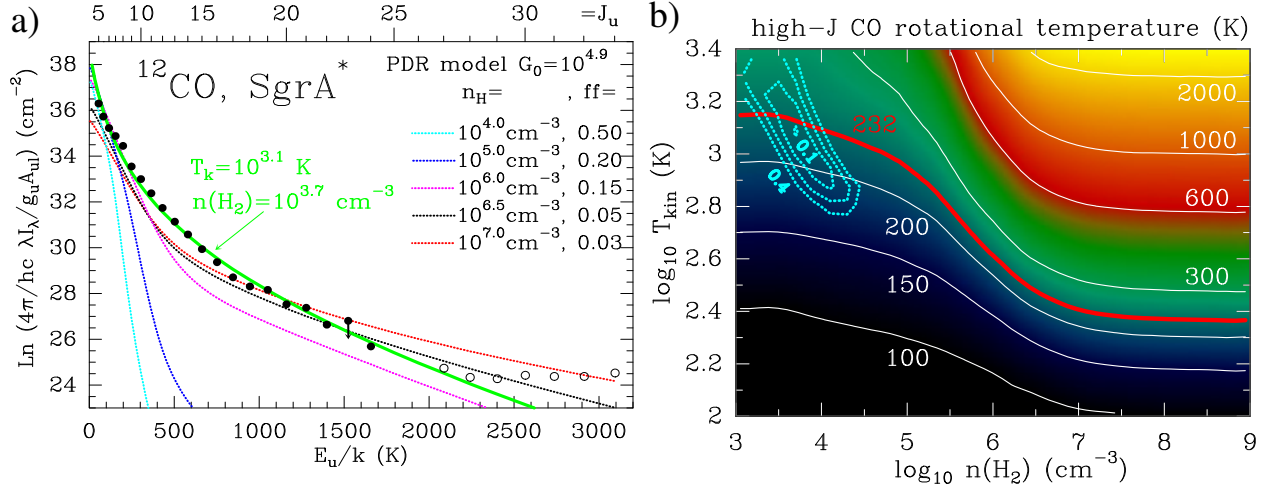


Fig. 3.— (a) Observed ^{12}CO rotational diagram for Sgr A* (filled circles). Open circles correspond to 3σ upper limits for non-detections. The green curve represents the best-fit isothermal model with $N(^{12}\text{CO}) = 10^{18} \text{ cm}^{-2}$. Dashed curves show rotational diagrams from PDR models with different filling factors ($I_{\text{obs}} = \text{ff} \cdot I_{\text{PDR}}$). (b) Synthetic CO rotational temperatures ($J_u = 14\text{--}24$ range) obtained from a grid of isothermal non-LTE models. Cyan contours show the rms levels of $\log_{10}(I_0/I_{\text{model}})$ for fits to the absolute line intensities from 0.1 (best-fits with a rms error of $\sim 25\%$) to 0.4 in rms error steps of 0.1.